First-Principles Investigation of the Structural Stability and Physical Properties of Lead-Free GE-Based Halide Perovskites

Liang Wang †, Longze Li †, Jiayin Zhang, Shuying Zhong, Bo Xu, Musheng Wu *, Chuying Ouyang

Posted Date: 18 August 2025

doi: 10.20944/preprints202508.1247.v1

Keywords: lead-free halide perovskite; structural stability; physical properties; first-principles calculations

 doi:10.20944/preprints202508.1247.v1

Article

First-Principles Investigation of the Structural Stability and Physical Properties of lead-Free Ge-Based Halide Perovskites

Liang Wang [1,†], Longze Li [2,†], Jiayin Zhang [1], Shuying Zhong [1], Bo Xu [1], Musheng Wu [1,2,*] and Chuying Ouyang [1]

[1] Physical Laboratory of Computational Materials, School of Physics and Communication Electronics, Jiangxi Normal University, Nanchang 330022, China

[2] 21C Innovation Laboratory, Contemporary Amperex Technology Ltd. (21C LAB) 352100, China

* Correspondence: smwu@jxnu.edu.cn

† These authors contributed equally to this work.

Abstract

Inorganic lead halide perovskite semiconductor materials exhibit great potential in the optoelectronic field due to their excellent optical and electrical properties. However, lead toxicity and limited material stability hinder their commercial applications. Consequently, the pursuit of non-toxic, stable alternatives is imperative for the sustainable development of halide-perovskite semiconductors. Non-toxic germanium-based halide perovskites, as promising candidates, have attracted considerable attention. Here, we present a systematic first-principles investigation of the structural, electronic, elastic, and optical properties of cost-effective germanium-based halide perovskites $NaGeX_3$ (X=Cl, Br, I). Energy and phonon-spectrum calculations demonstrate that $NaGeX_3$ with *R3c* space group exhibits the highest structural stability, rather than the commonly assumed cubic phase. Hybrid functional calculations reveal that the band gaps of *R3c* $NaGeX_3$ decrease monotonically with increasing halogen radius, that is, 4.75 eV ($NaGeCl_3$) → 3.76 eV ($NaGeBr_3$) → 2.69 eV ($NaGeI_3$), accompanied by a reduction in carrier effective masses. Additionally, mechanically stable *R3c* $NaGeX_3$ exhibits lower hardness and ductility than that with the cubic phase. Optical properties indicate that $NaGeX_3$ materials have strong absorption coefficients (> 10^6 cm^{-1}) and low loss in the photon energy range of 9-11 eV, suggesting that such cost-effective germanium-based halide perovskites can be used in various optoelectronic devices in the ultraviolet region.

Keywords: lead-free halide perovskite; structural stability; physical properties; first-principles calculations

1. Introduction

In recent years, lead halide perovskite semiconductor material $APbX_3$ (A is an univalent organic cation or alkali metal ion, X is a halogen ion such as Cl, Br, I) has attracted extensive attention due to its unique properties. $APbX_3$ presents excellent physical properties such as adjustable band gap [1], high defect tolerance [2], high absorption coefficient [3], carrier diffusion length [4] and long life [5], making it widely used in fields such as LEDs (LED) [6], photonic crystal lasers [7], photodetectors [8] and solar cell devices [9]. $APbX_3$ materials mainly consist of organic-inorganic and all-inorganic components according to the different A-site ions. For organic-inorganic mixtures such as $MAPbX_3$ ($MA=CH_3NH_3^+$), although the combination of the different properties of organic and inorganic components makes it easier to achieve wideband gap adjustment [10], the poor thermal stability of the organic cation (which decomposes easily in air and ultraviolet light) limits its large-scale application [11]. As a result, researchers began replacing organic cations with the inorganic metal ion

 doi:10.20944/preprints202508.1247.v1

Cs^+ to construct all-inorganic lead perovskite materials. It was found that all-inorganic perovskite materials exhibit higher stability than organic-inorganic hybrid lead perovskite materials [12], as solar cell materials, their photoelectric conversion efficiency exceeds 22% [13]. Therefore, all inorganic materials have attracted widespread attention.

Although all-inorganic lead halide perovskites have made considerable progress over the past decade and exhibit high conversion efficiency, they are harmful to the environment due to the toxic effects of Pb. Therefore, finding perovskite materials that can substitute for Pb while maintaining comparable carrier mobility and light absorption coefficient is crucial for the application of halide perovskites. To address this issue, researchers have attempted to regulate the composition of $APbX_3$ with non-toxic or low-toxic metal elements (e.g, Ti, Sn, Sb, Ge, Bi) [14,15]. Among these elements, Ge (in the same group as Pb) is considered a promising candidate. On the one hand, Ge exhibits similar electronic properties to Pb, thus showing comparable optoelectronic characteristics. In contrast, Sn, another element from the same group, is harmful to the human body. Moreover, $ASnX_3$ is prone to oxidation from Sn^{2+} to Sn^{4+} when exposed to air, thereby reducing the device's photovoltaic efficiency [16]. On the other hand, compared to Pb-based materials, germanium halide perovskite also has a better band gap value for solar cells [17–20], higher light absorption and light conductivity [21], showing greater potential in the photovoltaic field. For example, Chen [22] reported that $CsGeX_3$ with a uniform quantum rod (QR) structure achieves a power conversion efficiency of 4.92%, thereby enhancing its light absorption and charge transport capabilities.

In addition, $CsGeX_3$ can maintain the crystal structure and performance stability in high-temperature environments, is not prone to decomposition or phase transitions, and exhibits good resistance to environmental factors such as oxygen and moisture in the air, reducing performance degradation caused by chemical reactions and extending the service life of the material [23]. Furthermore, the high light absorption coefficient and long carrier diffusion length of $CsGeX_3$ enable it to efficiently absorb photons and generate electron-hole pairs in optoelectronic devices. Meanwhile, these carriers can be efficiently transported within the material, thereby enhancing the photoelectric conversion efficiency of the devices [24]. Subsequently, numerous research groups have conducted modification research on $CsGeX_3$ materials. On the one hand, research teams have enhanced the crystalline quality, purity, and electrical/optical properties of $CsGeX_3$ materials by optimizing the reaction system, precisely controlling synthesis parameters, and introducing specific additives [25]; on the other hand, the band structure and carrier transport characteristics of the materials can be effectively adjusted by proper doping of some elements in $CsGeX_3$. For example, doping the Ge element with equivalent or heterovalent ions introduces new energy levels, the electron distribution within the material is changed, and its optical and electrical properties are thereby affected [26].

Despite the numerous advantages of $CsGeX_3$ materials, the Cs element in $CsGeX_3$ is a rare metal priced at approximately 402.45 CNY/g (as shown in Figure 1), and the high cost will restrict its large-scale application in the semiconductor field. In contrast, Na, which belongs to the same main group as Cs, is one of the metal elements with abundant reserves on Earth. Its price is as low as 0.005 CNY/g (as shown in Figure 1), offering significant cost advantages and helping to reduce the production cost of Ge-based perovskite materials. Therefore, from the perspective of cost-effectiveness, especially in large-scale production and commercial applications, sodium has higher economic efficiency and feasibility. In addition, compared with $CsGeX_3$, $NaGeX_3$ has an impact on the lattice structure and ionic conduction due to the smaller ionic radius of Na than that of Cs, resulting in less hindrance during carrier transport in the $NaGeX_3$ system. This provides $NaGeX_3$ with higher ionic mobility and better performance in application scenarios requiring fast ionic conduction. However, research on $NaGeX_3$-type materials is scarce so far; in particular, there have been no experimental reports, and only a few studies have explored their geometric structures and physical properties [27,28]. The photoelectric properties of $NaGeX_3$ materials remain unclear, which significantly hinders the exploration of the diversity of $NaGeX_3$-based material systems and their application potential.

 doi:10.20944/preprints202508.1247.v1

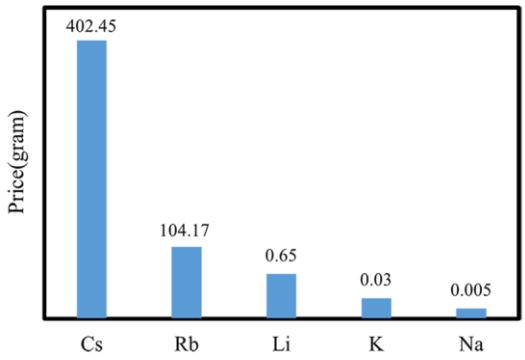

Figure 1. Price Chart of A-site Alkali Metal Elements in Ge-based Perovskite Materials.

To expand the halide perovskite material system and predict the physical properties of novel halide perovskites, we conducted a systematic first-principles calculation based on density functional theory (DFT) to investigate the structural stability, electronic, elastic, and optical properties of $NaGeX_3$ (X=Cl, Br, I) perovskite materials. By calculating the decomposition energies of various space groups ($Pm\bar{3}m$, *Pmna*, *R3m*, *R3c*), we found that $NaGeX_3$ with the *R3c* space group exhibits the highest decomposition energy, thereby confirming its superior thermodynamic stability. Additionally, to unveil the physical characteristics of *R3c* $NaGeX_3$, we systematically computed their band structures, elastic modulus, dielectric constants, refractive indices, reflectance spectra, and absorption coefficients. The results suggest that $NaGeX_3$ materials hold significant potential for applications in ultraviolet sensors and photoelectric conversion devices.

2. Calculation Methods

All calculations in this work were performed using first-principles methods based on Density Functional Theory (DFT), implemented with the VASP and DS-PAW software packages [29,30]. The interaction between ionic cores and valence electrons was described using the Projector-Augmented Wave (PAW) method [30] with a plane-wave cutoff energy of 500 eV. Electron-electron exchange and correlation effects were treated using the Perdew-Burke-Ernzerhof (PBE) [31] functional. Structural relaxation and static calculations for all systems were carried out using the DS-PAW software. Since the GGA method underestimates the band gap of materials, the more accurate hybrid density functional (HSE06) [32,33] was employed to calculate the density of states and band structures. *k*-point sampling of the first Brillouin zone was performed using the Monkhorst-Pack method [34] centered at the Γ point, and 7×7×7, 11×11×11, and 15×15×15 *k*-point grids were used for structural relaxation, electronic structure, and optical properties, respectively. Phonon dispersion relations were computed using density functional theory (DFT) combined with the finite displacement method, utilizing a 2×2×2 supercell (containing 80 atoms). The valence electron configurations of Na, Ge, Cl, Br, and I are $2p^6 3s^1$, $4s^2 4p^2$, $3s^2 3p^5$, $4s^2 4p^5$, and $5s^2 5p^5$, respectively. All atoms in the unit cell were fully relaxed, with a convergence precision of 10^{-5} eV for relaxation and a maximum interionic force of 0.01 eV/Å.

3. Results and Discussion

3.1. Structural Stability

It is first necessary to evaluate the structural stability of the $NaGeX_3$ materials due to the absence of extant experimental data. Generally, the tolerance factor (τ) proposed by Goldschmidt [35] based on oxide perovskites, as shown in Eq. (1), can be used to assess the stability of the perovskite structure in metal halide ABX_3 materials:

$$\tau = \frac{R_A + R_X}{\sqrt{2}(R_B + R_X)} \quad , (1)$$

 doi:10.20944/preprints202508.1247.v1

where R_A, R_B, and R_X are the effective ionic radii of the A-site, B-site, and X-site ions, respectively. Generally, the lower the tolerance factor τ, the lower the structural symmetry index, and vice versa. A stable perovskite structure is formed when τ falls within the range of [0.75, 1]. In other words, if τ<0.75 or τ>1, it is difficult to form a stable perovskite structure due to the A-site cation being too small or too large, which will transform into ilmenite and calcite configurations, respectively. When 0.75<τ<1, a value of τ close to 1 results in an ideal cubic perovskite structure; the greater the deviation from 1, the more severe the distortion of the BX_6 octahedron and the lower the structural symmetry, which tends to form orthorhombic, rhombic, or trigonal crystal structures [36]. Typically, to ensure the stability and symmetry of the octahedral structure, the ionic radius of the B-site cation is smaller than that of the A-site cation. Six X-site anions surround the B-site cation to form a BX_6 octahedral crystal, and these crystals form a three-dimensional structure through apex-sharing. The calculated τ values of $NaGeX_3$ are listed in Table 1. All three compounds exhibit τ values within the range of [0.75, 1], indicating that they can all form stable perovskite structures. On the other hand, their τ values all deviate from 1, making it difficult to form a cubic structure. From this perspective, $NaGeX_3$ with the cubic phase reported in the literature [27,37] should, in principle, be unstable.

Table 1. Tolerance factor (τ), lattice constants, and band gap (E_g) of *R3c* for $NaGeX_3$.

Halide	LC/Å				E_g/eV		
	R3c	*Pm$\bar{3}$m*	*Pmna*	*R3m*	Our work GGA/HSE06	Other work GGA [28]	τ
$NaGeI_3$	*a*=7.90, *c*=22.48	*a*=5.90	*a*/*b*/*c*=4.41/ 11.05/16.32	*a*/*b*/*c*=8.63/ 8.56/7.71	2.00/2.69	2.00	0.86
$NaGeBr_3$	*a*=7.50, *c*=21.42	*a*=5.49	*a*/*b*/*c*=4.16/ 11.00/13.71	*a*/*b*/*c*=8.41/ 7.74/9.23	2.83/3.76	2.79	0.88
$NaGeCl_3$	*a*=7.25, *c*=20.44	*a*=5.20	*a*/*b*/*c*=3.98/ 10.79/12.65	*a*/*b*/*c*=8.32/ 7.58/9.20	3.74/4.75	3.72	0.89

To determine the ground-state structure of the $NaGeX_3$, the stability of these phases was evaluated using decomposition energy (E_{decomp}) for four commonly reported space groups of halide perovskites, namely *Pm$\bar{3}$m*, *Pmna*, *R3m* and *R3c* [27,28,37,38]. E_{decomp} can be calculated via Eq. (2):

$$E_{\text{decomp}}=E_{eq}(C)-E(NaGeX_3)\ , \quad (2)$$

where $E_{eq}(C)$ denotes the total energy of all decomposed components C at equilibrium; $E(NaGeX_3)$ represents the total energy of $NaGeX_3$ with different space groups. $E_{decomp}\geq 0eV$ indicates that the structure is stable at 0 K; otherwise, it tends to decompose into other component compounds, i.e., instability. However, generally, $E_{decomp}>-25$ meV/atom, the phase is considered a metastable phase with a high probability of experimental synthesis, considering the contribution of entropy and the kinetic barrier to decomposition [39,40].

Based on the data from the Open Quantum Materials Database (OQMD) [41] and our DFT calculation results, the ternary phase diagrams of Na-Ge-X at 0 K were constructed, as shown in Figures 2(a), 2(b), and 2(c). Herein, only thermodynamically stable compounds are displayed. It can be seen from the Na-Ge-X ternary phase diagrams that the direct decomposition products of $NaGeX_3$ compounds are NaX and GeX_2. Therefore, for the calculation of the decomposition energy of $NaGeX_3$, we only consider the phase equilibrium reaction according to Eq. (3):

$$NaGeX_3\rightarrow NaX+GeX_2\ , \quad (3)$$

 doi:10.20944/preprints202508.1247.v1

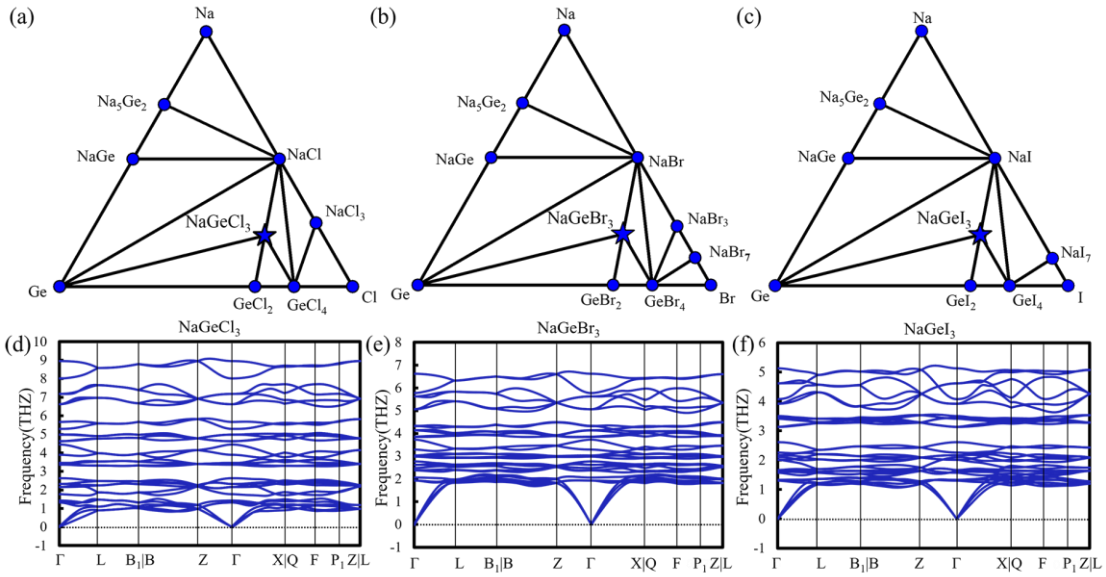

Figure 2. Ternary phase diagrams (**a**-**c**) and phonon spectra (**d**-**f**) of $NaGeX_3$ (X=Cl, Br, I), blue dots representing stable compounds of Na-Ge-X and pentagrams representing.

To accurately evaluate the thermodynamic stability of $NaGeX_3$ across all phases, we first determined the ground-state structures and energies of the four phases. Using the DS-PAW software, we constructed models for all $NaGeX_3$ phases ($Pm\bar{3}m$, *Pmna*, *R3m*, and *R3c*) and performed DFT relaxation for these structures. The relaxed lattice constants are listed in Table 1, and the atomic structures are shown in the inset of Figure 3(a). As shown in Table 1, the lattice constants increase with the halide ionic radius due to the weakening of Ge-X covalent bonds. The calculated lattice constants for the $Pm\bar{3}m$ and *R3c* phases using the GGA functional are consistent with literature values [27,28], validating the reliability of our computational models and parameters. Next, we calculated the energies of the corresponding decomposition products, NaX and GeX_2. For $GeCl_2$, which has not been experimentally synthesized, we used the *C2/c* space group structure from the OQMD database as the decomposition product for $NaGeCl_3$. For $GeBr_2$ and GeI_2, we obtained their structures from the Inorganic Crystal Structure Database (ICSD): $P12_1/c1$ phase for $GeBr_2$ and $P\bar{3}m1$ phase for GeI_2. The crystal structures of GeX_2 are illustrated in Figure 3(b).

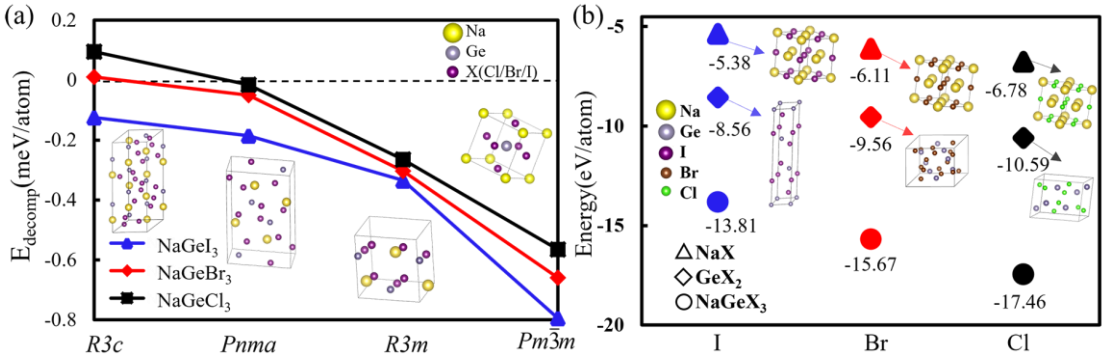

Figure 3. (**a**) Decompound energies of $NaGeX_3$ with different phases. (**b**) the corresponding decomposition products of *R3c* $NaGeX_3$.

As can be seen from Figure 3(a), among the four structures of $NaGeX_3$, the type of halogen has almost no effect on the stability trend of the materials. Specifically, for $NaGeCl_3$, $NaGeBr_3$, and $NaGeI_3$, the *R3c* phase exhibits the largest decomposition energy, which are 0.09 meV/atom, 0 meV/atom, and -0.13 meV/atom, respectively. The corresponding decomposition energies of the other

 doi:10.20944/preprints202508.1247.v1

three phases are all smaller than that of the *R3c* phase, with the $Pm\bar{3}m$ phase showing the lowest value. This indicates that the *R3c* phase is the most stable, especially for $NaGeCl_3$ and $NaGeBr_3$, which is consistent with the calculation results of the tolerance factor, i.e., it is difficult to form a cubic structure. For the *R3c* phase of $NaGeI_3$, although its decomposition energy is negative, the value of -0.13 meV/atom indicates that it is metastable. Considering the contribution of entropy, it will become stable at finite temperatures. To further confirm the stability of the *R3c* phase, we calculated the phonon spectra of the *R3c* phase, as shown in Figures 2(d), 2(e), and 2(f). It can be seen that there are no imaginary frequencies in the entire Brillouin zone, indicating that the *R3c* phase of $NaGeX_3$ is dynamically stable. Therefore, in subsequent studies, we only consider $NaGeX_3$ with the *R3c* phase.

To clearly reveal the geometric structure of $NaGeX_3$ with the *R3c* phase, we present its crystal structure in Figure 4. The *R3c*-phase $NaGeX_3$ belongs to the trigonal crystal, where X atoms and Ge atoms form an octahedron [GeX_6] with the Ge atom at the center. The Ge-X and Na-X bonds exhibit covalent and ionic characteristics, respectively. In this structure, adjacent $[GeX_6]^{4-}$ octahedrons share a halogen X atom and extend continuously in three directions through corner-sharing, forming a three-dimensional perovskite framework. Na^+ cations are interspersed in the interstitials of the octahedral framework $[GeX_6]^{4-}$. The radius of Na^+ cations (1.02Å) is less than 2.6Å, satisfying Goldschmidt's empirical rule, thus enabling $NaGeX_3$ to maintain the three-dimensional perovskite structure [42]. Given that three-dimensional perovskites exhibit strong and broad optical absorption, generate free carriers upon photoexcitation, and possess high carrier mobility and long carrier diffusion lengths, these properties make $NaGeX_3$ structurally suitable for optoelectronic devices, particularly photovoltaic devices.

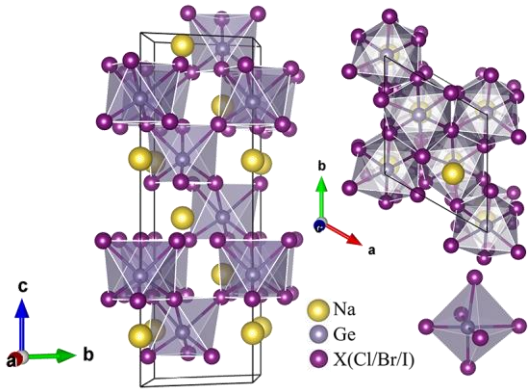

Figure 4. The relaxed structure of $NaGeX_3$(X=Cl, Br, I) with *R3c* phase using DS-PAW.

3.2. Electronic Structure

For semiconductor materials, electronic structure is a key factor determining their properties, and it is also crucial for understanding the nature of interatomic bonding, electrical conductivity, and optoelectronic properties. As is well-known, the GGA method underestimates the band gap of materials. To accurately evaluate the band gap of $NaGeX_3$ (X=Cl, Br, I), we calculated the band structures using the hybrid density functional (HSE06). The calculated band structures and density of states (DOS) are shown in Figure 5. The red horizontal dashed line at 0 eV represents the Fermi level (E_f). In Figure 5, the energy range displayed is -4 to 8 eV, which includes the valence band maximum (VBM) and conduction band minimum (CBM) regions. For all $NaGeX_3$ structures, the VBM is located at the Γ point. The difference is that the CBM of $NaGeBr_3$ and $NaGeCl_3$ is located at the F point, as shown in Figures 5(a) and 5(b), while the CBM of $NaGeI_3$ is also located at the Γ point. This indicates that the former two have indirect band gaps, whereas $NaGeI_3$ has a direct band gap. Therefore, the luminous efficiency of $NaGeI_3$ should be higher than that of the other two materials.

 doi:10.20944/preprints202508.1247.v1

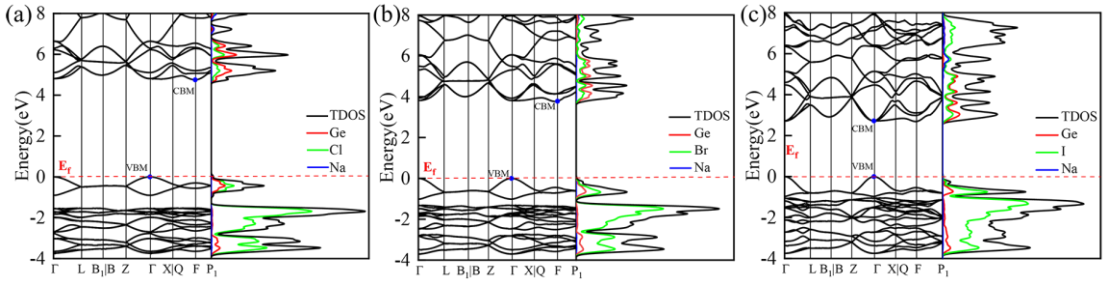

Figure 5. HSE06 calculated band structure and density of states of $NaGeX_3$(Cl, Br, I) (**a-c**).

The band gap values of all *R3c* phase $NaGeX_3$ calculated by HSE06 range from 2.69 to 4.75 eV, as listed in Table 1. For comparison with the literature, we also calculated the band gaps of all $NaGeX_3$ using the GGA method (Table 1). The GGA results are consistent with those reported in the literature [28], confirming the reliability of our calculations. Additionally, the GGA band gap values of all $NaGeX_3$ are approximately 1 eV smaller than those from HSE06, further verifying the underestimation of band gaps by GGA. For different halogens, it is found that the band gaps increase as the halogen atomic radius decreases, i.e., from 2.69 eV for $NaGeI_3$ to 3.76 eV for $NaGeBr_3$ and 4.75 eV for $NaGeCl_3$. This trend is mainly determined by the outermost p-orbital energy levels and electronegativity of the halogens. In perovskite material systems, an ideal band gap usually needs to balance efficient absorption of sunlight with effective generation and transport of carriers. Compared with some traditional perovskite materials, $NaGeI_3$, with a direct band gap of 2.69 eV, avoids the rapid non-radiative recombination that reduces photoelectric conversion efficiency in narrow-bandgap materials, while still maintaining sufficient sunlight absorption despite its slightly wider band gap. These characteristics lay a solid theoretical foundation for the application of $NaGeI_3$ in optoelectronic devices such as perovskite solar cells and photodetectors, making it a promising candidate for next-generation high-performance perovskite materials.

To gain a better understanding of the electronic properties of $NaGeX_3$, we calculated their total density of states (TDOS) and partial density of states (PDOS). As shown in Figure 5, all $NaGeX_3$ exhibit a similar electronic distribution. The valence bands are primarily contributed by Ge (4p) atoms and halogen X atoms (Cl 3p, Br 4p, I 5p), with the contribution of X to the VBM increasing as the halogen ionic radius increases. The CBMs are also mainly contributed by Ge and halogen X atoms, with Ge being the dominant contributor, while the 3s and 3p states of Na make little contribution. Notably, significant hybridization is observed between Ge and X in all halides, confirming the covalent nature of their chemical bonds. Additionally, based on the DOS of Na, it is expected that ionic bonds will form between Na and halogen X, which helps maintain the stability of the perovskite structure rather than participating in electronic transition processes. Thus, it can be concluded that the electronic transitions during photoexcitation primarily occur between the p orbitals of halogens and Ge atoms.

3.3. Effective Mass

Carrier effective mass (m^*) is another key parameter describing the electronic properties of semiconductor materials, and it is of great significance for understanding the electrical conductivity, optoelectronic properties, and thermoelectric properties of semiconductor materials. According to Eq. (4) [43], m^* is inversely proportional to the curvature of the material's energy bands. Therefore, based on the parabolic approximation, we calculated the effective masses of electrons (m_e) and holes (m_h) near the bottom of the CBM and the top of the VBM for all $NaGeX_3$ by fitting the dispersion relations:

$$m^* = \hbar^2 \left(\frac{\partial^2 E(k)}{\partial k^2}\right)^{-1} , \qquad (4)$$

where $\hbar$, k and $E(k)$ are the reduced planck constant, wave vector, and energy eigenvalue at the band edge, respectively. For the calculation of m_e and m_h, we performed a fine fitting on the band structures

 doi:10.20944/preprints202508.1247.v1

of the CBM and VBM around the Γ point, as these band structures exhibit obvious parabolic characteristics, as shown in Figure 5. The calculated average effective masses of carriers (with m_0 being the electron mass) for all $NaGeX_3$ along the Z→Γ and Γ→X directions are listed in Table 2. The results show that the average effective electron mass m_e of all $NaGeX_3$ materials is smaller than the effective hole mass m_h, indicating that the electron mobility is significantly higher than that of holes. Moreover, as the halogen ionic radius increases, the $m^*$of $NaGeX_3$ decreases. $NaGeI_3$ exhibits the smallest effective electron and hole masses, with average values of $0.42m_0$ and $0.58m_0$, respectively. This significant mass difference indicates that electrons are more mobile than holes, contributing to their high carrier mobility. In addition, $D=m_h/m_e$ is often used to describe the degree of carrier recombination; a higher D value indicates that electron-hole pairs are more likely to separate [44], thereby reducing the carrier recombination rate.

Table 2. The average carrier effective masses of $NaGeX_3$ along the Z→Γ and Γ→X directions.

Halide	m_e (m_0)			m_h (m_0)			D=m_h/m_e		
	Z-Γ	Γ-X	AVG	Z-Γ	Γ-X	AVG	Z-Γ	Γ-X	AVG
$NaGeI_3$	0.39	0.45	0.42	0.65	0.50	0.58	1.67	1.11	1.39
$NaGeBr_3$	0.76	0.82	0.79	0.64	1.90	1.27	0.84	2.32	1.58
$NaGeCl_3$	1.51	1.46	1.49	0.86	3.56	2.21	0.57	2.44	1.50

3.4. Mechanical Properties

The mechanical properties of solids not only help explain the response mechanism of interatomic potentials to external forces but also play a crucial role in various fundamental phenomena of solid-state materials (such as stability, strength, ductility, brittleness, and other characteristics). These properties include parameters such as Young's modulus (Y), bulk modulus (B), shear modulus (G), anisotropy factor, and other elastic parameters, providing an important basis for exploring the behavioral characteristics of materials under different conditions. The elastic constants and modulus of all $NaGeX_3$ were calculated and listed in Table 3 based on the relationship between the two [45]. For comparison, the counterparts of cubic $NaGeX_3$ calculated by Pingak et al [27] were also listed in Table 3.

Based on the mechanical stability criteria proposed by Gao et al [46], all trigonal $NaGeX_3$ materials are mechanically stable because their C_{ij} values satisfy the following criteria: $C_{44}>0$, $C_{11}-|C_{12}|>0$, $C_{33}(C_{11}+C_{12})-2C_{13}^2>0$, and $C_{44}(C_{11}-C_{12})-2C_{14}^2>0$. Additionally, for all trigonal $NaGeX_3$, $NaGeI_3$ possesses the highest hardness and stiffness, owing to the maximum Young's modulus (E=10.88 GPa), Bulk Modulus (B=6.21 GPa), and shear modulus (G=4.5 GPa), indicating that $NaGeI_3$ has the strongest resistance to mechanical deformation among the three materials, while $NaGeBr_3$ is the most sensitive to external stress due to the lowest elastic modulus (E=7.1, B=3.75, and G=3). However, compared with the corresponding cubic structures, the elastic moduli of all trigonal $NaGeX_3$ are smaller, as listed in Table 3, indicating that the trigonal cases are soft materials with lower hardness and stiffness, more suitable for scenes requiring slight mechanical stability (eg, thin-film devices).

The Pugh's ratio (B/G) and Poisson's ratio (ϑ) are related to the ductility and brittleness of materials. A material is ductile if the Pugh's ratio is greater than 1.75; otherwise, it is brittle [47]. Similarly, a higher Poisson's ratio (> 0.26) indicates better ductility [45]. As shown in Table 3, all three trigonal materials exhibit brittleness due to their B/G and ϑ being less than 1.75 and 0.26, respectively, with $NaGeBr_3$ having the highest brittleness. In contrast, all cubic cases possess ductility, with $NaGeCl_3$ having the highest ductility owing to the greatest B/G (2.45) and ϑ (0.32). This result indicates that, compared to cubic structures, trigonal $NaGeX_3$ materials are not suitable as flexible devices.

 doi:10.20944/preprints202508.1247.v1

Table 3. Calculated elastic properties of *R3c*-phase $NaGeX_3$(X = Cl, Br, and I).

Elastic Parameters	This Work for *R3c*			Other Work for $Pm\bar{3}m$ [27]		
	$NaGeCl_3$	$NaGeBr_3$	$NaGeI_3$	$NaGeCl_3$	$NaGeBr_3$	$NaGeI_3$
C_{11} (GPa)	10.52	8.91	13.65	57.89	50.78	41.11
C_{12} (GPa)	3.80	2.55	4.05	10.96	8.64	6.32
C_{13} (GPa)	2.32	1.70	2.94	/	/	/
C_{14} (Gpa)	-0.90	-0.50	-1.16	/	/	/
C_{33} (GPa)	6.72	5.33	9.70	/	/	/
C_{44} (GPa)	4.03	3.21	4.68	6.11	5.79	5.57
B (GPa)	4.79	3.75	6.21	20.26	22.69	17.92
E (GPa)	8.33	7.10	10.88	28.57	22.11	23.00
G (GPa)	3.44	3.00	4.50	10.86	10.03	8.98
B/*G*	1.39	1.25	1.38	2.45	2.26	2.00
ϑ	0.21	0.18	0.21	0.32	0.31	0.27

3.5. Optical Properties

The dielectric function (ε) is a crucial parameter for the optical properties of materials, as it contains information about the material's response to incident photons. It serves as a core bridge connecting the microscopic electronic responses of materials to macroscopic optical properties such as absorption (α), reflection (R), and refraction (n). The complex form of the dielectric function [48] can be expressed as follows:

$$(\omega) = \varepsilon_1(\omega) + i\varepsilon_2(\omega) \quad (5)$$

$\varepsilon_1(\omega)$ and $\varepsilon_2(\omega)$ represent the real and imaginary parts of the dielectric function, respectively. Other optical properties such as absorption (α), reflection (R), refraction (n), and extinction coefficient (k) can be calculated from the obtained ε_1 and ε_2. For detailed calculation formulas, please refer to the literature [49].

Figure 6 presents the calculated dielectric constants, absorption coefficients, refractive indices/extinction coefficients, and reflectivity/loss of the three $NaGeX_3$ materials as functions of photon energy within the energy range of 0-20 eV. Figures 6(a) and 6(b) show the variation curves of the real part $\varepsilon_1(\omega)$ and imaginary part $\varepsilon_2(\omega)$ of the dielectric function with incident photon energy. It can be seen from the figures that the static dielectric constant $\varepsilon_1(0)$ increases with increasing halogen atomic radius. The $\varepsilon_1(0)$ values of $NaGeCl_3$, $NaGeBr_3$, and $NaGeI_3$ are 3.34, 4.01, and 5.68, respectively, as listed in Table 4. This result is reasonable because according to the Penn model [50], $\varepsilon_1(0) = 1 + (\hbar\omega_p/E_g)^2$, where a smaller band gap corresponds to a larger $\varepsilon_1(0)$. Moreover, starting from the zero-frequency limit, the ε_1 of all $NaGeX_3$ begins to increase, reaches a maximum within the energy range of [2,5] eV, then starts to decrease, drops to a negative value around 10 eV, and finally fluctuates slowly with higher photon energies. Overall, in the energy range of 0-10 eV, the ε_1 of $NaGeX_3$ materials changes rapidly as the incident light energy gradually increases; when the incident light energy exceeds 10 eV, the change rate of the real part of the dielectric function slows down significantly and gradually becomes stable.

 doi:10.20944/preprints202508.1247.v1

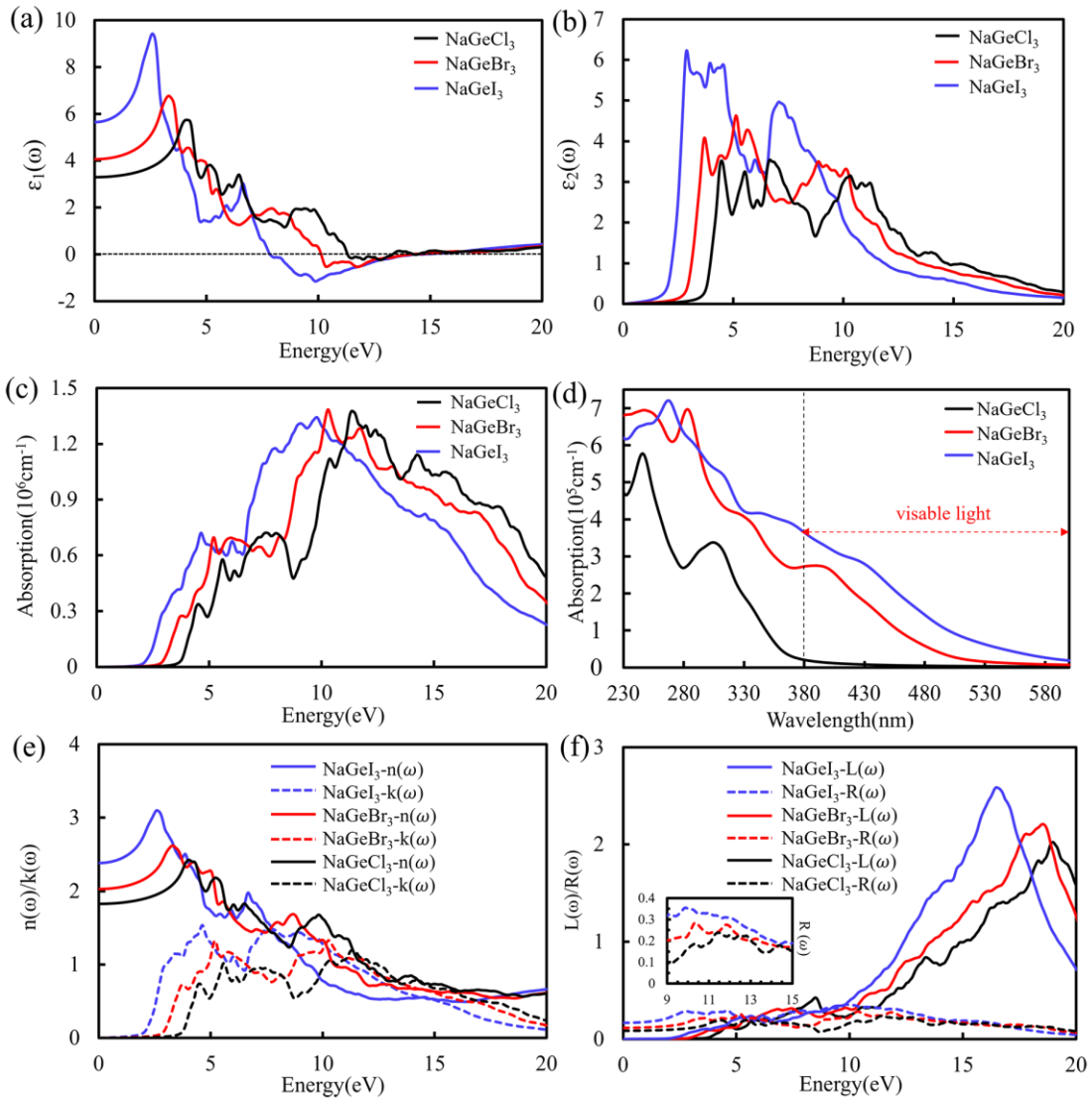

Figure 6. (**a**,**b**) Dielectric function; (**c**,**d**) Absorption coefficient; (**e**) Refractive index $n(\omega)$ and Extinction coefficient $k(\omega)$; (**f**) Reflection spectrum $R(\omega)$ and Loss function $L(\omega)$ for $NaGeX_3$(X=Cl, Br, I).

Table 4. Calculated frequency independent dielectric constant $\varepsilon_1(0)$, refractive index n(0), and reflectivity R(0) of $NaGeX_3$(X=Cl, Br, I).

Compounds	$\varepsilon_1(0)$	n(0)	R(0)
$NaGeI_3$	5.68	2.38	0.17
$NaGeBr_3$	4.01	2.03	0.12
$NaGeCl_3$	3.34	1.83	0.09

The value of the imaginary part of the dielectric function ε_2, arises from electron transitions from the top of the valence band to the bottom of the conduction band, determining the linear response of the system to light at small wave vectors. Its peak value can reflect the intensity of electron excitation transitions in the material; a larger peak indicates a stronger electron absorption capacity. As shown in Figure 6(b), the absorption edge of ε_2 for all compounds is located at the band gap position of their respective materials, and the absorption edge increases with the increase of halogen radius, indicating that $NaGeI_3$ has the strongest absorption. As the incident light energy increases, the number of states where electrons can undergo transitions increases. Within the energy range of 0-13 eV, the ε_2 of $NaGeX_3$ changes rapidly, showing first and second peaks and the subsequent changes

 doi:10.20944/preprints202508.1247.v1

are relatively slow. Combined with the analysis of electronic structure, it is known that the first peak originates from electron transitions between the p orbitals of halogen X and the 4p orbitals of Ge.

Based on the dielectric function, the absorption coefficient $\alpha(\omega)$ of $NaGeX_3$ was further calculated, which can directly quantify the material's ability to absorb light. The variation of $\alpha(\omega)$with photon energy is illustrated in Figure 6(c). As shown in the figure, within the energy range of 0-20 eV, the absorption coefficient of $NaGeI_3$ reaches a maximum value of 1.34×10^6 cm^{-1} at $\hbar\omega$=9.77 eV; while $NaGeBr_3$ and $NaGeCl_3$ reach the same maximum value of 1.38×10^6 cm^{-1} at $\hbar\omega$= 10.27 eV and 11.37 eV, respectively. The three materials exhibit weak absorption in the visible light range ($\hbar\omega$=1.65-3.26 eV). When the photon energy exceeds that of visible light, the absorption coefficient reaches a large order of magnitude (10^6 cm^{-1}) over a wide range of photon energies, mainly showing ultraviolet absorption. Figure 6(d) presents the relationship between the absorption spectrum and wavelength. When Cl is replaced by I, the absorption spectrum undergoes a red shift, and $NaGeI_3$ exhibits a higher absorption coefficient, which exceeds 7×10^5 cm^{-1} near a wavelength of 280 nm. In the figure, the region with a wavelength less than 380 nm is the ultraviolet region, and that greater than 380 nm is the visible light region. It can be inferred that these three materials may be ideal for manufacturing ultraviolet sensors, and $NaGeBr_3$ and $NaGeI_3$ may be applicable to the fabrication of blue-light lasers. Compared with the other two, $NaGeI_3$ has superior light absorption performance in the visible range. In addition, the refractive index $n(\omega)$ and extinction coefficient $k(\omega)$ are important optical parameters describing the interaction between light and matter. The refractive index n determines the path and direction of light propagation in different media, while the extinction coefficient k represents the energy attenuation of light propagating in the material. Figure 6(e) shows the refractive index $n(\omega)$ and extinction coefficient $k(\omega)$ of $NaGeX_3$. As can be seen from Figure 6(e) and Table 4, the static refractive indices n(0) of $NaGeCl_3$, $NaGeBr_3$, and $NaGeI_3$ are 1.83, 2.03, and 2.38, respectively. The photon energies corresponding to the maximum peaks of the refractive index n are 4.2 eV, 3.4 eV, and 2.74 eV, respectively, and the refractive index gradually decreases with further increase in photon energy. A larger static refractive index n(0) essentially reflects a stronger polarization ability of the material under static conditions, which is specifically manifested as more significant electron cloud distortion, easier ion displacement, or higher free carrier concentration. Thus, $NaGeI_3$ exhibits more excellent properties. Furthermore, the extinction coefficient k of $NaGeI_3$, $NaGeBr_3$, and $NaGeCl_3$ is greater than the refractive index n in the energy ranges of 7.79-14.75 eV, 10.12-13.87 eV, and 11.26-13.35 eV, respectively. This is because within these energy ranges, the real part of the dielectric function $\varepsilon_1 < 0$, meaning that the wave vector K is imaginary, i.e., light in these ranges cannot propagate in $NaGeX_3$.Corresponding to the absorption coefficient, the extinction coefficients of $NaGeCl_3$, $NaGeBr_3$, and $NaGeI_3$ all gradually decrease when the energy exceeds around 10 eV, and eventually approach zero near 20 eV. At this point, the incident light frequency is greater than or equal to the natural oscillation frequency, and the optical quantities characterizing solid absorption all approach zero. The refractive index varies with frequency as normal dispersion (the refractive index decreases with increasing frequency), and the extinction coefficient exhibits strong absorption characteristics at the band edge.

To further investigate the energy loss during electron excitation under photon interaction, we calculated the relationships of the loss function and reflectivity of $NaGeX_3$ with photon energy, as shown in Figure 6(f). The results indicate that although the loss functions of the three materials contain two loss peaks within the range of material light absorption (9-11 eV), their values are relatively low. Moreover, the maximum reflectivity of $NaGeX_3$ in the energy range of 9-11 eV, i.e., the ultraviolet region, does not exceed 36%. This suggests that $NaGeX_3$ materials have little impact on the absorption of photons; in other words, ultraviolet light can more easily enter such germanium-based halide perovskite materials.

In summary, the low-cost Ge-based halide perovskite material $NaGeX_3$ exhibits strong absorption and low loss in the ultraviolet region, showing potential for application in ultraviolet sensing and optoelectronic devices. Compared with the other two materials, $NaGeI_3$ requires lower photon energy to reach the maximum light absorption intensity, with its absorption peak redshifted

 doi:10.20944/preprints202508.1247.v1

and the wavelength of absorbed light lengthened. This indicates that $NaGeI_3$ can more efficiently capture photons in the long-wavelength or visible light regions, providing more sufficient carriers for optoelectronic devices and thus holding certain potential as a perovskite solar cell material.

4. Conclusions

In this paper, first-principles calculations based on density functional theory were employed to systematically investigate the geometric structures, electronic, elastic, and optoelectronic properties of $NaGeX_3$ (X = Cl, Br, I). Among the four space groups, the *R3c* phase $NaGeX_3$ structure exhibits the highest thermodynamic and dynamic stability. Studies on the electronic and optical properties of the *R3c* phase $NaGeX_3$ reveal that the valence band maximum and conduction band minimum of $NaGeX_3$ (X = Cl, Br, I) are dominated by the p-orbitals of halogens and Ge, respectively. Additionally, the band gap of the material decreases with increasing halogen atomic radius. Furthermore, the absorption coefficient reaches a maximum of 1.38×10^6 cm^{-1} within the photon energy range of 9-11 eV, and the absorption spectrum redshifts as the halogen radius increases. This study indicates that $NaGeX_3$ holds promising application prospects in fields such as ultraviolet sensing and photoelectric conversion devices.

Funding: This work is supported by the National Natural Science Foundation of China (12464029, 12174162), the Natural Science Foundation of Jiangxi Province (20232BAB201030, 20242BAB25034). This work was performed on the Hongzhiwei Cloud platform and Tianhe new generation supercomputer at the National Supercomputing Center in Tianjin, thank to Hongzhiwei and Tianhe for their strong support.

Data Availability Statement: The original contributions presented in this study are included in the article. Further inquiries can be directed to the corresponding author.

Conflicts of Interest: The authors declare no conflicts of interest.

References

1. Wei, S. H.; Yan, Y. F.; Yin, W. J. Anomalous Alloy Properties in Mixed Halide Perovskites. *J. Phys. Chem. Lett.* **2014**, 5, 3625.
2. Yin, W. J.; Shi, T.T.; Yan, Y.F. Unique Properties of Halide Perovskites as Possible Origins of the Superior Solar Cell Performance. *Adv. Mater.* **2014**, 26, 4653.
3. Yin, W. J.; Shi, T.; Yan, Y. Unusual defect physics in $CH_3NH_3PbI_3$ perovskite solar cell absorber. *Appl. Phys. Lett.* **2014**, 104, 063903.
4. Turedi, B.; Lintangpradipto, M. N.; Sandberg, O. J.; Yazmaciyan, A.; Matt, G. J.; Alsalloum, A. Y.; Almasabi, K.; Sakhatskyi, K.; Yakunin, S.; Zheng, X.; Naphade, R.; Nematulloev, S.; Yeddu, V.; Baran, D.; Armin, A.; Saidaminov, M. I.; Kovalenko, M. V.; Mohammed, O. F.; Bakr, O. M. Single-Crystal Perovskite Solar Cells Exhibit Close to Half A Millimeter Electron-Diffusion Length. *Adv. Mater.* **2022**, 34, e2202390.
5. Chen, R. H.; Zhuang, B.; Lin, J. D.; Pang, T.; Zeng, L. W.; Chen, D. Q. Ultralong Decay Lifetime for $CsPbBr_3$ Perovskite Quantum Dots Glass. *Adv. Optical Mater.* **2025**, 13, e01385.
6. Yuan, Y.; Xu, R.; Xu, H. T.; Hong, F.; Xu, F.; Wang, L. J. Nature of the band gap of halide perovskites ABX_3 (A= CH_3NH_3, Cs; B= Sn, Pb; X= Cl, Br, I): First-principles calculations. *Chin. Phys. B* **2015**, 24, 116302.
7. Li, X. M.; Wang, Y.; Sun, H. D.; Zeng, H. Amino-Mediated Anchoring Perovskite Quantum Dots for Stable and Low-Threshold Random Lasing. *Adv. Mater.* **2017**, 29, 1701185.
8. Sun, H. X.; Tian, W.; Cao, F.; Xiong, J.; Li, L. Ultrahigh-Performance Self-Powered Flexible Double-Twisted Fibrous Broadband Perovskite Photodetector. *Adv. Mater.* **2018**, 30, e1706986.
9. Lin, W. H.; Canton, S. E.; Zheng, K.; Pullerits, T. Carrier Cooling in Lead Halide Perovskites: A Perspective on Hot Carrier Solar Cells. *ACS Energy Lett.* **2023**, 9, 298.
10. Thatribud, A.; Rassamesard, A. Electronic and optical properties of lead halide perovskite ($MAPbX_3$) (X = I, Br, and Cl) by first principles calculations. *Phys. Scr.* **2022**, 97, 110245.

 doi:10.20944/preprints202508.1247.v1

11. Schwenzer, J. A.; Hellmann, T.; Nejand, B. A.; Hu, H.; Abzieher, T.; Schackmar, F.; Hossain, I. M.; Fassl, P.; Mayer, T.; Jaegermann, W.; Lemmer, U.; Paetzold, U. W. Thermal Stability and Cation Composition of Hybrid Organic-Inorganic Perovskites. *ACS Appl. Mater. Interfaces* **2021**, 13, 15292.
12. Niu, G.; Guo, X.; Wang, L. Review of recent progress in chemical stability of perovskite solar cells. *J. Mater. Chem. A* **2015**, 3, 8970.
13. Li, R.; Zhang, S.; Zhang, H.; Wang, Z.; Feng, X.; Du, Y.; Zhou, T.; Chen, X.; Liu, P.; Liu, L.; Zhang, J.; Chen, Q.; Xi, L.; Zhao, K.; Liu, S. F.; Tian, Q. Customizing Aniline-Derived Molecular Structures to Attain beyond 22% Efficient Inorganic Perovskite Solar Cells. *Angew. Chem. Int. Ed.* **2024**, 63, e202410600.
14. Hui, W.; Kang, X. X.; Wang, B. H.; Li, D. L.; Su, Z. H.; Bao, Y. Q.; Gu, L.; Zhang, B.; Gao, X. Y.; Song, L.; Huang, W. Stable Electron-Transport-Layer-Free Perovskite Solar Cells with over 22% Power Conversion Efficiency. *Nano Lett.* **2023**, 23, 2195-2202.
15. Zhu, T.; Yang, Y.; Gong, X. Recent Advancements and Challenges for Low-Toxicity Perovskite Materials. *ACS Appl. Mater. Interfaces* **2020**, 12, 26776.
16. Muntasar, A.; Roux, D. L.; Denes, G. Stabilization of the unhybridized Sn^{2+}, stannous ion in the BaClF structure and its characterization by 119 Sn Mössbauer spectroscopy. *J. Radioanal. Nucl. Ch.* **1995**, 190, 431-437.
17. Hamideddine, I.; Tahiri, N.; Bounagui, O. E.; Ez-Zahraouy, H. Ab initio study of structural and optical properties of the halide perovskite KBX_3 compound. *J. Korean Ceram. Soc.* **2022**, 59, 350.
18. Pandey, M.; Jacobsen, K. W.; Thygesen, K. S. Band Gap Tuning and Defect Tolerance of Atomically Thin Two-Dimensional Organic–Inorganic Halide Perovskites. *J. Phys. Chem. Lett.* **2016**, 7, 4346.
19. Ming, W.M.; Shi, H.; Du, M.H. Large dielectric constant, high acceptor density, and deep electron traps in perovskite solar cell material $CsGeI_3$. *J. Mater. Chem. A* **2016**, 4, 13852.
20. Krishnamoorthy, T.; Ding, H.; Yan, C.; Leong, W. L.; Baikie, T.; Zhang, Z.; Sherburne, M.; Li, S.; Asta, M.; Mathews, N.; Mhaisalkar, S. G. Lead-free Germanium Iodide Perovskite Materials for Photovoltaic Application. *J. Mater. Chem. A* **2015**, 3, 23829.
21. Roknuzzaman, M.; Ostrikov, K.; Wang, H.; Du, A.; Tesfamichael, T. Towards lead-free perovskite photovoltaics and optoelectronics by ab-initio simulations. *Sci. Rep.* **2017**, 7, 14025.
22. Chen, L. J. Synthesis and optical properties of lead-free cesium germanium halide perovskite quantum rods. *RSC Adv.* **2018**, 8, 18396-18399.
23. Chen, C. C.; Kuai, Y.; Li, X.; Hao, J. B.; Li, L.; Liu, Y.; Ma, X. G.; Wu, L. Y.; Lu, P. F. Impact of Halogen Substitution on the Electronic and Optical Properties of 2D Lead-Free Hybrid Perovskites. *J. Phys. Chem. C* **2021**, 125, 15742.
24. Ikram, M.; Malik, R.; Raees, R.; Imran, M.; Wang, F.; Ali, S.; Khan, M.; Khan, Q.; Maqbool, M. Recent advancements and future insight of lead-free non-toxic perovskite solar cells for sustainable and clean energy production: A review. *Sustain. Energy Technol. Assess.* **2022**, 53, 16.
25. Chen, R.; Luo, B.; Liu, C.; Ma, X. N.; Qiao, L.; Yao, B. X.; Gao, R. L.; Feng, Z. J.; Liu, J.; Lin, H.; Kong, X. Y.; Ren, W. Polarization Controlled Photocurrent in Perovskite $CsGeX_3$ (X = Cl, Br, I). *J. Phys. Chem. C* **2023**, 39, 19788.
26. Zhang, C.; Wang, H.; Huang, W.; Zuo, Y.; Cheng, J. A Systematical Study on Bands and Defects of $CsBX_3$ (B = Pb, Sn, Ge, X = Cl, Br, I) Perovskite Based on First Principles. *MOLECULES* **2024**, 29, 2479.
27. Pingak, R. K.; Bouhmaidi, S.; Setti, L. Investigation of structural, electronic, elastic and optical properties of Ge-halide perovskites $NaGeX_3$ (X = Cl, Br and I): A first-principles DFT study. *Phys. B* **2023**, 663, 415003.
28. Luo, Y.R.; Tian, H.; Li, X.; Chen, L.; Yang, Y.; Wu, D. Diversity of structural phases in $AGeX_3$ halides. *Phys. Rev. B* **2022**, 106, 024112.
29. Kresse, G.; Joubert, D. Efficient iterative schemes for ab initio total-energy calculations using a plane-wave basis set. *Phys. Rev. B* **1999**, 59**,** 1758.
30. Blochl, P. E. Projector augmented-wave method. *Phys. Rev. B* **1994**, 50, 17953.
31. Perdew, J. P.; Burke, K.; Ernzerhof, M. Generalized Gradient Approximation Made Simple. *Phys. Rev. Lett.* **1996**, 77, 3865.
32. Heyd, J.; Scuseria, G. E.; Ernzerhof, M. Hybrid functionals based on a screened Coulomb potential. *Chem. Phys.* **2003**, 118, 8207.

 doi:10.20944/preprints202508.1247.v1

33. Chen, H.; Li, M.; Wang, B.; Ming, S.; Su, J. Structure, electronic and optical properties of $CsPbX_3$ halide perovskite:A first-principles study. *J. Alloys Compd.* **2021**, 862, 158442.
34. Chadi, D. J. Special points for Brilloofn-zone integrations. *Phys. Rev. B* **1977**, 16, 1746.
35. Kieslich, G.; Sun, S.; Cheetham, A. K. An extended Tolerance Factor approach for organic–inorganic perovskites. *Chem. Sci.* **2015**, 6, 3430.
36. Yi, Z.J.; Ladi, N. H.; Shai, X. Will organic – inorganic hybrid halide lead perovskites be eliminated from optoelectronic applications?. *Nanoscale Adv.* **2019**, 1, 1276.
37. Ovi, I. A.; Hasan, M. R.; Apon, I. A.; Zahra, F. T. Pressure-driven semiconducting to metallic transition in francium tin trihalides perovskite with improved optoelectronic performance: A DFT study. *Mater. Res. Express* **2024**, 11, 065904.
38. Sarker, M. A.; Muntasir, M.; Momin, M. A.; Solayman, M.; Islam, M. R. Pressure-Induced Structural, Electronic, and Optical Properties of Lead-Free $NaGeX_3$(X = F, Cl, Br, and I) Perovskites: First-Principles Calculation. *Adv. Theory Simul.* **2024**, 7, 2400112.
39. Sun, W. H.; Dacek, S. T.; Ong, S. P.; Hautier, G.; Jain, A.; Richards, W. D.; Gamst, A. C.; Persson, K.A.; Ceder, G. The thermodynamic scale of inorganic crystalline metastability. *Sci. Adv.* **2016**, 2, e1600225.
40. Bartel, C. J.; Millican, S. L.; Deml, A. M.; Rumptz, J. R.; Tumas, W.; Weimer, A. W.; Lany, S.; Stevanović, V.; Musgrave, C. B.; Holder, A. M. Physical descriptor for the Gibbs energy of inorganic crystalline solids and temperature-dependent materials chemistry. *Nat. Commun.* **2018**, 9, 4168.
41. Kirklin, S.; Saal, J. E.; Meredig, B.; Thompson, A.; Doak, J .W.; Aykol, M.; Rühl, S.; Wolverton, C. The Open Quantum Materials Database (OQMD): assessing the accuracy of DFT formation energies. *NPJ Comput. Mater.* **2015**, 1, 15010.
42. Grancini, G.; Nazeeruddin, M.K. Dimensional tailoring of hybrid perovskites for photovoltaics. *Nat. Rev. Mater.* **2019**, 4, 22.
43. Tripathi, G. S.; Shadangi, S. K. Many-body theory of effective mass in degenerate semiconductors. *Int. J. Mod. Phys. B* **2018**, 32, 1850082.
44. Ompong, D.; Inkoom, G.; Singh, J. Effective mass of heavy, light, and spin split-off band electron and hole g-factor in cubic perovskite materials. *J. Appl. Phys.* **2020**, 128, 235109.
45. Ghaithan, H. M.; Alahmed, Z. A.; Qaid, S. M. H.; Aldwayyan, A. S. Density functional theory analysis of structural, electronic, and optical properties of mixed-halide orthorhombic inorganic perovskites. *ACS Omega* **2021**, 6, 30752.
46. Gao, J.; Jiang, C. L.; Fan, D. H.; Zhang, M.; Liu, F. S.; Tang, B. Criteria of Mechanical Stability of Seven Crystal Systems and Its Application: Taking Silica as an Example. *Chin. J. High Press. Phys.* **2022**, 36, 051101.
47. Pugh, S. F. Relations between the elastic moduli and the plastic properties of polycrystalline pure metals, London, Edinburgh Dublin Phil. *Philos. Mag.* **1954**, 45, 823-843.
48. Lu, C. L.; Zhang, L.; Zhang, Y. W.; Liu, S. Y.; Mei, Y. Electronic, optical properties, surface energies and work functions of Ag8SnS6: First-principles method. *Chin. Phys. B* **2015**, 24, 017501.
49. Rai, D. P.; Shankar, A.; Sakhya, A. P.; Sinha, T. P.; Merabet, B.; Khenata, R.; Boochani, A.; Solaymani, S.; Thapa, R. K. Electronic and optical properties of cubic SrHfO3 at different pressures: A first principles study. *Mater. Chem. Phys.* **2017**, 186, 620.
50. Penn, D. R. Wave-Number-Dependent Dielectric Function of Semiconductors. *Phys. Rev.* **1962**, 128, 2093.